# Enhanced Energy Dissipation in Periodic Epoxy Nanoframes

Jae-Hwang Lee,[†,§] Lifeng Wang,[†] Steven Kooi,[§] Mary C. Boyce,[†,§] and Edwin L. Thomas*[,†,§]

[†]Department of Materials Science and Engineering, [‡]Department of Mechanical Engineering, and [§]Institute for Soldier Nanotechnologies, Massachusetts Institute of Technology, Cambridge, Massachusetts 02139

**ABSTRACT** Periodic nanostructures fabricated by interference lithography can be precisely designed to have a specific cell geometry, topology, and porosity in contrast to typical stochastic cellular materials. We use nanoindentation to elucidate the mechanical characteristics of the nanoframe as a function of its relative density and model the deformation behavior via numerical simulations. The nanoframe exhibits a scaling exponent of relative modulus versus relative density of 1.26, which is less sensitive than for conventional foams. Moreover, the nanoframe shows large mechanical energy dissipation/volume (up to 4.5 MJ/m$^3$), comparable to the highest values achieved in the conventional polymer foams but at a far smaller strain. Counterintuitively, a nanoframe of smaller relative density can dissipate more energy per volume because the geometry of the nanoframe evolves during deformation to engage more of the material in plastic deformation. The results demonstrate how geometrical control at the nano- and microstructural scale can tailor modulus and energy dissipation and suggest means for engineering of mechanically superior materials in the future.

**KEYWORDS** Mechanical properties, periodic nanostructure, epoxy, interference lithography

Despite major advances in the enhancement of the mechanical properties of materials, the control of these properties still relies largely on bulk processing to influence the material's microstructure. This is equally true for cellular (or porous) structures, which are generally produced by stochastic processing with a range of open and closed cell geometries and sizes.[1−4] Recently, by fabricating randomly porous metals, stronger materials are possible due to the nanoscale dimensions of the ligaments.[5−7] Ordered cellular structures can offer opportunities to engineer a set of physical properties including optical,[8,9] thermal,[10,11] acoustic[12,13] as well as chemical properties[14,15] by virtue of their high specific surface area/volume and fluidic permeability. A relatively new class of cellular materials, holographically defined nanoframes has been fabricated by light-induced cross-linking of photoresists using interference of multiple laser beams (interference lithography).[9,16,17] Unlike traditional cellular materials, the cell geometry and topology of the holographic periodic nanoframes can be rationally designed. Interference lithography gives precise control of the geometry, scale and volume fraction of the microstructure while post exposure baking and flood illumination gives control of the cross-link density of the material. The cross-link density combined with the length scale, geometry and porosity of the structures, tailor and determine the system's overall mechanical behavior. Thus, nanoframes made by interference lithography may lead to improved mechanical properties beyond specific stiffness including enhanced energy absorption and fracture toughness, which are in demand to develop smart structures for response to specific stress conditions (e.g., advanced personnel protection armor).[18]

There have been several preliminary mechanical property studies of periodic bicontinuous polymer nanoframes,[19−24] but as yet, no systematic experimental study as a function of relative density ($\rho_R$). Here, we elucidate how the mechanical characteristics depend on $\rho_R$, including anisotropic deformation, elastic moduli, the elastic deformation limit, plastic deformation modes, and energy dissipation. The nanoframe structures show transitions in both elastic and plastic responses as a function of $\rho_R$, originating from their unique holographically defined topology, which allows a nanoframe of a lower $\rho_R$ to absorb more energy per unit volume than those of a higher $\rho_R$ at a fixed structural periodicity when subject to the same loading conditions. Moreover, we find that the dissipated energy per unit volume in compression of our periodic nanoframes is substantially larger than that of conventional polymer foams at the same compressive strain.

A photocross-linkable epoxy resin (SU-8, Microchem) was chosen to fabricate epoxy nanoframes using multiple beam interference lithography because SU-8 shows a relatively uniform dose throughout the film due to its very low absorption in the near-UV range.[25] Moreover, the cross-linked epoxy exhibits good chemical resistance, thermal and mechanical properties, and has been extensively used as a structural material in MEMS devices and as a matrix in various composite materials.[26] We spin coat SU-8 monomer onto a precross-linked SU-8 buffer layer film supported by a glass substrate. A three-dimensional (3D) latent chemical image is then formed within the top SU-8 layer by interference lithography[16] using four ultraviolet (UV) laser beams

* To whom correspondence should be addressed. E-mail: elt@mit.edu. Phone: (617) 253-6901. Fax: (617) 252-1175.
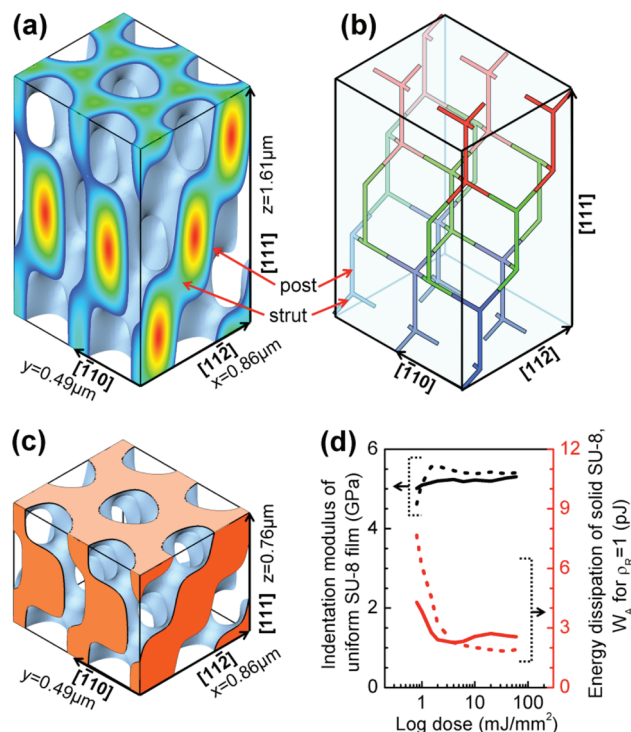
**FIGURE 1. Schematic of the nanoframe structure fabricated by interference lithography. (a) The isointensity surface of four-beam laser interference in a SU-8 layer for $\rho_R$ of 0.5 is shown with the interior strut intensity profiles at the boundaries of the cells. The figure has $1 \times 2$ cells bounded by the (111), (11$\bar{2}$), and ($\bar{1}$10) planes. In the intensity profile of the $xz$-plane (b) a skeletal graph shows the connectivity of the iso-intensity surface with basic structural motif consisting of six thin lateral struts and a thicker single vertical post. Each layer of the motifs along [111] is depicted with different color. (c) A structure after 47% vertical shrinkage as defined by contraction of $z$-coordinates of the original iso-intensity surface. (d) Indentation modulus and energy dissipation of uniform SU-8 films as a function of 355 nm UV dose before (dashed lines) and after (solid lines) the extra 365 nm UV flood exposure with a dose of 120 mJ/mm² and bake.**

($\lambda = 355$ nm) from a frequency-tripled Nd:YAG laser. In the configuration of the four beams, a circularly polarized center beam is incident perpendicular to the surface of the SU-8 layer. Three side beams are equally spaced around the azimuth, are linearly polarized in transverse magnetic mode, and are tilted 56° to the film surface normal to minimize reflection at the air-SU-8 and SU-8-glass interfaces. A 3D latent chemical image is formed in the SU-8 monomer layer by the 4-beam interference. Figure 1a shows the iso-intensity surface of the 4-beam laser interference for an array of $1 \times 2$ unit cells. The isointensity structure in SU-8 layer has $R3$ symmetry with the in-plane periodicity (along [11$\bar{2}$]) equal to 0.86 $\mu$m with the periodicity along the film surface normal (along [111]) equal to 1.61 $\mu$m. To better depict the topology of the structure, a skeletal graph of the nanoframe is shown in Figure 1b. The basic motif consists of a thick vertical post with six (3 oriented upward and 3 downward) obliquely oriented thin struts. The structure has 3-fold symmetry along the $z$-axis ([111], the main strut axis). After exposure, the sample is then baked to initiate cross-linking in the high

exposure areas, and the uncross-linked areas are subsequently washed out in a development process. A nanoframe on a substrate undergoes a large vertical shrinkage during processing (40−60%) because of photopolymerization and solvent development steps.[27] As a result, an actual nanoframe has a smaller $z$-axis repeat as depicted in Figure 1c and the space group transforms to $R32$.[28] Thus, the final epoxy nanoframe will have a periodicity along [111] ranging from 1.1 to 0.8 $\mu$m depending on $\rho_R$.

Ideally $\rho_R$ can be controlled by varying the exposure dose. However, the actual value of $\rho_R$ is a combined result of the exposure dose and the vertical shrinkage, inversely proportional to the exposure dose. We determine $\rho_R$ via measurement of the effective refractive index ($n_{eff}$) of a nanoframe using the Bruggemann effective medium approximation,[29] $\rho_R(n_{SU8}^2 - n_{eff}^2)/(2n_{eff}^2 + n_{SU8}^2) = (1 - \rho_R)(n_{eff}^2 - n_{air}^2)/(2n_{eff}^2 + n_{air}^2)$. Reflectance measurements in the mid-infrared range ($\lambda = 3-7$ $\mu$m) allow determination of $n_{eff}$, since each nanoframe can be considered as an effective medium due to the sufficiently large wavelength of light relative to the nanoframe feature size. The theoretical range of $\rho_R$ from the isointensity surface that defines the bicontinuous distribution of solid and pore space varies from 0.2 to 0.8, however the experimentally attainable range of $\rho_R$ is approximately 0.5 to 0.75 because the thin struts are unstable at lower $\rho_R$ due to the low contrast of the strut relative to the matrix background (e.g., see the strut region in Figure 1a) and due to the densification of the structures by the vertical shrinkage.

In addition, we also take into account the dose dependence of mechanical properties. The exposure dose to vary $\rho_R$ results in different cross-link densities, and moreover due to the local variation of light intensity (see Figure 1a) even within a given structure, there is a variation in cross-link density.[20] Thus, UV dose dependent mechanical properties of SU-8 should be studied as well as the properties that are dependent on $\rho_R$ of nanoframes. We employ a nanoindentation technique (TI900 TriboIndenter, Hysitron Inc.) to test solid SU-8 films and nanoframes. The maximum loads (0.6 and 1.2 mN) are applied by a diamond spherical indenter, 10 $\mu$m radius, with the same rate of loading and unloading (60 $\mu$N/sec). For purposes of comparing the different materials, an effective indentation modulus can be calculated by the Oliver−Pharr model[30,31] from the unloading curve. First, we evaluate the properties of uniform SU-8 films. As seen in Figure 1d, the indentation modulus of the uniform SU-8 films exposed to 355 nm UV starts at about 4.5 GPa and reaches a maximum of 5.4 GPa at a dose of 2 mJ/mm². We also calculated energy dissipation ($W_A$), the area enclosed by loading and unloading curves, as an indicator of plastic deformation during loading. As expected, the plasticity of the uniform SU-8 films is more sensitive to cross-linking than the modulus since the material is in its glassy state at room temperature for all cross-link densities ($T_g > 100$ °C).[21] The loss of plasticity at higher doses causes the energy dissipation to drop rapidly and saturates to a rather small value
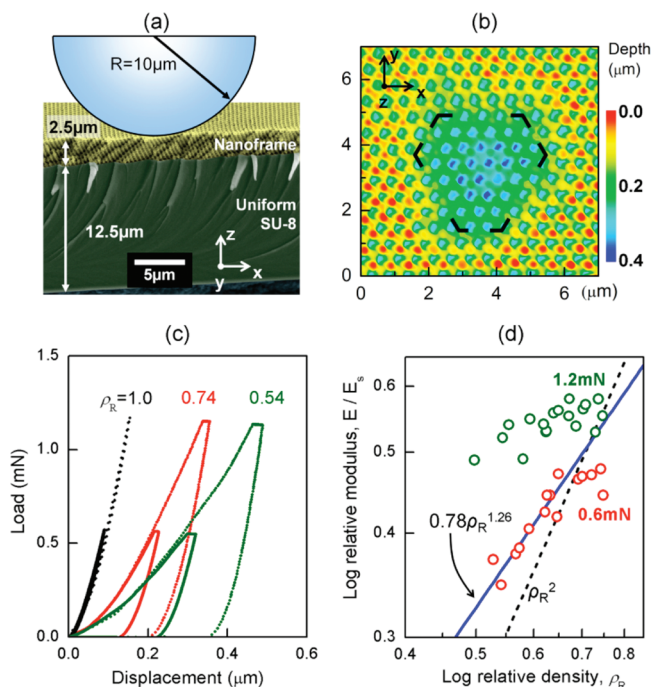
FIGURE 2. Indentation tests for the set of (fully) cross-linked samples with variable relative density. (a) Scanning electron microscope (SEM) micrograph with a schematic of the 10 $\mu$m radius spherical indenter. A 2.5 $\mu$m thick nanoframe is supported by a uniform 12.5 $\mu$m thick SU-8 film. (b) AFM height image of the residual indentation by a 1.2 mN load applied for 10 s (image was taken after about 60 days). (c) Selected load–displacement curves with maximum loads of 0.6 and 1.2mN (loading rate of 60 $\mu$N/sec) versus volume fraction of cross-linked SU-8 nanoframe. (d) The relative moduli of nanoframes for the two different maximum loads, 0.6 (red circle) and 1.2 mN (green circle) are shown with a fitting curve to the 0.6 mN-data for $\rho_R < 0.65$. For reference, the quadratic scaling curve (dashed line) is also plotted.

($\sim$25% of the value of the lowest dose). Indeed, the films with the highest cross-link density are nearly fully elastic at these loads as evidenced by the unloading curve retracing the loading curve and also evidenced by atomic force microscope (AFM) inspection of the SU-8 film after indentation which shows no residual depression. The differences in mechanical responses resulting from variable cross-link densities in SU8 can be greatly reduced by an additional flood exposure ($\lambda = 365$ nm) at a dose of 120 mJ/mm$^2$, followed by an hour-long bake at 75 °C (for the nanoframes this treatment is done after the development step).

The spherical indenter has a contact area covering at least 30 unit cells over the top surface, so the applied contact pressure is predominantly along the $z$-axis (sample surface normal) as seen in the to-scale-schematic (Figure 2a). Indentation (0.6 or 1.2 mN) leaves a residual surface depression on the nanoframe as shown in the AFM height image in Figure 2b. Interestingly, an outline of the residual indent is not circular, reflecting the anisotropic nature of the nanoframe. The imprint is an equiangular 6-sided polygon (but not a hexagon) consistent with the 3-fold symmetry about the $z$-axis as seen in Figure 1b. Representative load–displace-

ment curves are shown in Figure 2c for different $\rho_R$. In general, for the same loads, the load–displacement curves of nanoframes show elastic-plastic deformation while a similarly cross-linked homogeneous SU-8 film displays a negligible amount of plastic deformation. The relative indentation moduli $E^*(\rho_R)/E_S$ are plotted in Figure 2d, where $E_S$ and $E^*(\rho_R)$ are the indentation modulus of the reference cross-linked SU-8 film and the $\rho_R$-dependent indentation modulus of nanoframes, respectively. The moduli derived from the larger load of 1.2 mN are not sensitive to $\rho_R$ and give higher values than those determined from the 0.6 mN load. This is because the moduli are calculated from the elastic recovery of plastically deformed densified nanoframes that have an effectively higher relative density and a somewhat distorted structure than the initial undeformed structure as well as from the larger elastic contribution from the underlying homogeneous SU-8 layer. Therefore, the moduli determined from the lower maximum load provide a better measure of the intrinsic properties of the nanoframe. The relative modulus is 0.45 for the nanoframe with the largest value of $\rho_R$ of 0.75; in other words, introducing 25% of air space results in a 55% decrease in modulus. This modulus reduction relative to a uniform SU-8 film is primarily due to the cellular structure but is also influenced by the leaching of oligomers during development of the nanoframe epoxy prior to the final flood exposure and long bake. The relative modulus of cellular solids have been found (in the limit of low $\rho_R$) to scale as $E^*/E_S \sim \rho_R^n$. A scaling exponent $n$ close to 1 indicates stretch-dominated deformation behavior of the struts whereas a quadratic exponent typically indicates bending-dominated deformation.[32] Various cellular materials have been found to exhibit different scaling exponents such as metal foams ($n \sim 1$–3),[2] silica aerogel ($n \sim 3.7$),[33] ordered nanoporous silica ($n \sim 0.6$–1),[4] while an anisotropic natural cellular material like cork has $n \sim 1$ for the axial direction and $n \sim 3$ for the radial direction.[34] Our nanoframe results show a slope of 1.26 for $\rho_R < 0.65$ and a smaller slope for densities above $\rho_R$. A transition in the dissipative behavior of the nanoframes at this same relative density was also observed. These transitions indicate a change in the underlying deformation mechanisms once $\rho_R$ exceeds 0.65.

The indent load–unload curves for the nanoframe material (Figure 2c) reveal the elastic-plastic nature of the indentation behavior for these indent loads. The dependence of the plasticity on $\rho_R$ is further studied by examining the dependence of the degree of residual deformation (DRD) and $W_A$ as a function of $\rho_R$. The manner in which the DRD depends on $\rho_R$ (see Figure 3a) can provide an indicator of plasticity. Here we define the DRD as the residual indentation volume normalized to its maximum indentation volume, (the volume of material displaced by the 10 $\mu$m radius sphere at its maximum distance into the sample). In contrast to a negligible DRD of the solid SU-8 material, the nanoframes exhibit a large DRD that is proportional to the porosity, $1 - \rho_R$. This means, as expected, that the more porous
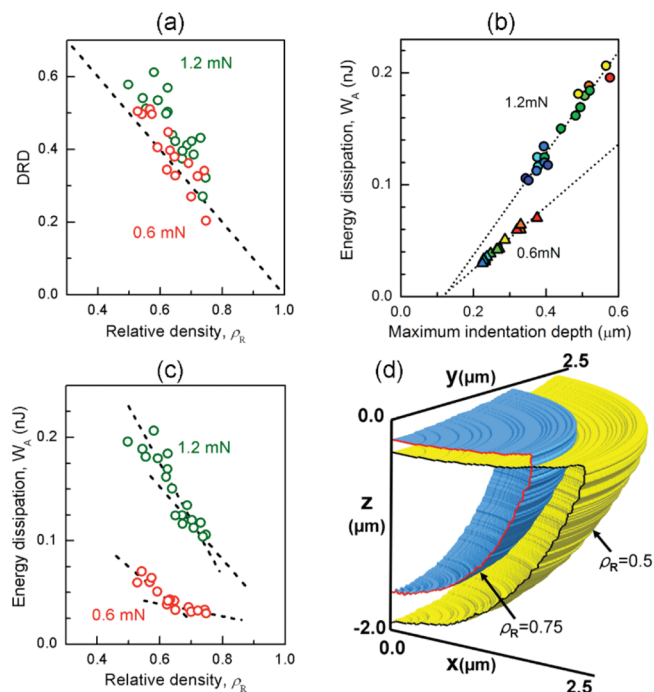
**FIGURE 3.** Assessment of plastic deformation in the nanoframes. (a) Degree of residual deformation (DRD) is plotted for the two different maximum loads with $1 - \rho_R$ line (dashed). (b) Dissipation as a function of maximum indentation depth for the two maximum loads. A warmer fill color represents higher $\rho_R$ and dashed lines are linear fitting curves. (c) Energy dissipation by plastic deformation of a nanoframe is shown as a function of $\rho_R$ for the two different maximum loads, 0.6 and 1.2mN. (d) A quadrant view of the calculated volumes of the plastic zone under a load of 0.6mN by a 10 $\mu$m radius spherical indenter, where the plastic zone is defined by the volume having more than 2% plastic strain.

materials undergo larger plastic deformation at a given load. We also see the data from 1.2 mN load have higher DRD because a deeper indentation within a finite thickness nanoframe causes more plastic deformation. Figure 3b shows how the energy dissipation characteristics depend on the maximum indentation depth. It is clear that $W_A$ has a linear dependence with the maximum indentation depth and the dependency is larger for the higher maximum load due to the nonlinearity of deformation and the greater influence of the finite-thickness of nanoframes at higher loads. However, the linear fitting curves for the two sets of data have nearly the same value of $x$-intercept (110 nm), which indicates the nanoframes do not provide plastic energy dissipation when the indentation depth is below ~5% of total nanoframe thickness regardless of $\rho_R$.

The $W_A$ plot of nanoframes in Figure 3c shows more energy is dissipated at lower $\rho_R$; specifically there is a more than 200% increase in energy absorption by reducing $\rho_R$ from 0.75 to 0.5 for the two maximum loads, which is consistent with the trend of DRD with $\rho_R$ in Figure 3a. This is because $W_A$ is associated with plastic deformation. Moreover, $W_A$ is rapidly increased as the volume fraction of solid drops below 0.65. Although the $W_A$ transition is due to dissipation, this trend is related to the indentation modulus

transition observed earlier in Figure 2d, where both are governed by a change in deformation mechanism at this volume fraction.

To explore the elastic-plastic indentation of the nanoframe films, we employ an axisymmetric finite element analysis (FEA) model of the indentation process. The FEA model is composed of an effective nanoframe layer of thickness 2.5 $\mu$m (approximately two unit cells thick) and a fully dense buffer layer of thickness 12.5 $\mu$m. The upper nanoframe layer was assumed to possess isotropic elastic-porous plastic constitutive behavior[35] with material properties determined by fitting the two-layer model to the experimental data. The FEA model accounts for the finite thickness of the nanoframe layer and the influence of the substrate on the indentation behavior and hence provides a more accurate means to isolate the effective properties of the nanoframe layer. From the FEA simulations, the volume of the plastic zone at the maximum load of 0.6 mN can be calculated for different $\rho_R$. For instance, in Figure 3d, the volumes of the plastic zones are ~17 and 8 $\mu$m$^3$ for $\rho_R$ of 0.5 and 0.75, which are 20 times larger than their corresponding maximum residual indentation volumes. With this information on the plastic zones, we can estimate an energy dissipation density ($W_A$/volume of plastic zone) although we do recognize that the plastic strain is not uniform over this volume. Indentation to a load of 0.6 mN gives an energy dissipation density for $\rho_R = 0.75$ of 3.6 MJ/m$^3$ compared to a value of 4.5 MJ/m$^3$ for $\rho_R = 0.5$. This result seems counterintuitive as less material dissipates more energy, but the situation is that a nanoframe having a lower $\rho_R$ has a 3D geometry more conducive to plastic deformation. Moreover, the demonstrated energy dissipation value for this direction of loading, 4.5 MJ/m$^3$ with an estimated nanoframe/air density of 0.6 g/cm$^3$, rates among the highest values reported for conventional isotropic polymer foams[3] even though the average effective strain of the nanoframe in these cases is approximately 10%. This energy dissipation capability implies of the nanoframe structure can be tuned to provide dissipation mechanisms that engage more of the material in plastic deformation than found in more traditional cellular structures where bending and hinged plasticity may be dominant.

To understand the local deformation mechanisms leading to the modulus transition and the dissipation transition, we performed linear elastic calculations of vertically contracted nanoframe models under uniaxial compressive stress.[36] The von Mises stress contours in Figure 4, normalized to that of a uniform solid under the same stress, show how the stress distribution evolves as $\rho_R$ is reduced. Besides a general trend in the maximum and overall stress levels being inversely proportional to $\rho_R$, there is a dramatic dependence of the distribution in the high-stress regions on $\rho_R$. Larger $\rho_R$ nanoframes (Figure 4a) show a relatively more uniform distribution of stress throughout the structure indicating that these materials can be deformed by the applied compressive
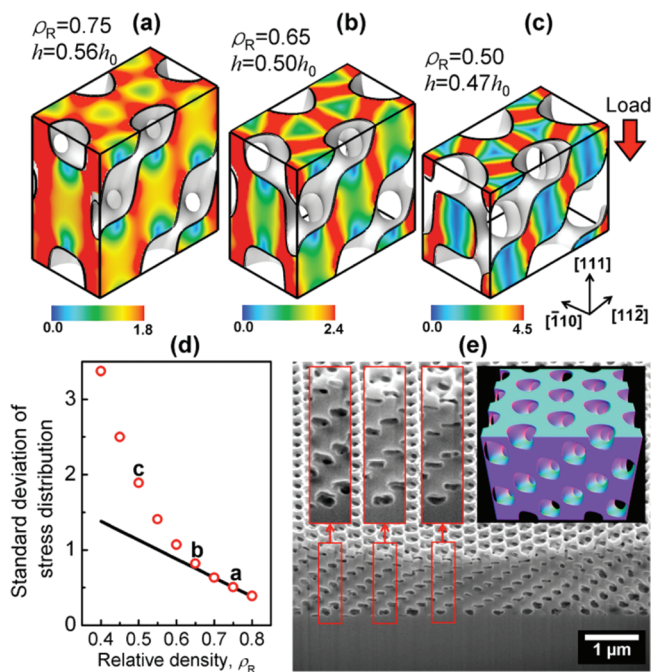
**FIGURE 4.** Theoretical von Mises stress distributions of nanoframes for three values of $\rho_R$, (a) 0.75, (b) 0.65, and (c) 0.50, respectively, under a same compressive stress along the [111] direction. The level of stress is normalized to that of the 100% solid. The initial height of each unit cell ($h_0 \sim 1.61 \ \mu$m) is vertically contracted to reflect the experimentally observed shrinkage. (d) The standard deviation of the local stresses within a single unit cell as a function of $\rho_R$ represents the degree of concentration of the stress (red circle). The three deviations corresponding to the stress maps in (a–c) are marked with the same figure letters. A solid line is a linear fit for high $\rho_R$. (e) A cross-sectional SEM image (52° tilt) of a focused ion-beam milled nanoframe shown along with magnified images of three selected regions. The cross-section plane is (11$\bar{2}$). A corresponding cross-sectional model in the inset is generated by shifting the original unit cell (11$\bar{2}$) boundary face 75 nm along the [$\bar{1}$10] direction to reflect the actual SEM image.

load through shearing of the diagonal struts as well as compression of the vertical posts. In contrast, nanoframes with low $\rho_R$ (Figure 4c) show high stress regions localized in the diagonal struts indicating that these structures can be deformed by the applied compression through shearing of the diagonal struts. Nanoframes with $\rho_R$ close to the transition $\rho_R$ (Figure 4b) show an intermediate state. The stress contours do not suggest any form of bending mode. Therefore, the greater dissipation observed in these nanoframe structures when compared against those values for more conventional cellular materials lies in their ability to dissipate energy through plastic shearing of diagonal members as well as the vertical members. The stress concentration aspect of the distributions is explicitly shown in the standard deviation plot of stress distributions in Figure 4d. Because regions with higher stress-concentration initiate plastic deformation leading to large local strains, it is evident that a nanoframe with smaller $\rho_R$ will undergo more plastic deformation with accompanying higher energy dissipation at lower loads since the plasticity is initiated by yielding the smaller section of the diagonal struts via shear as opposed to the larger section

by compression. We also see that the standard deviation of stress distribution is exponentially increased for $\rho_R$ less than 0.65, which is in agreement with the transition point observed in modulus and energy dissipation. Thus, the trend in Figure 4d explains why the transition point exists, and how a nanoframe comprised of less material can dissipate more energy. To clearly show the positional dependence of the plastic deformation, we indented a nanoframe ($\rho_R$ = 0.54) to a much higher maximum load of 6 mN, and cross sectioned the center of the indent mark by focused ion beam milling (see Figure 4e). The vertical air gaps between posts are compressed far more than the height of the posts, indicating that shear-dominant deformation occurs primarily in the diagonal struts, as expected for nanoframe with a small $\rho_R$ (Figure 4c).

In summary, we examined how the mechanical properties of bicontinuous cross-linked polymer/air nanoframes depend on the volume fraction of solid using a nanoindentation technique. Periodic bicontinuous nanoframes show several distinctive mechanical characteristics compared to traditional randomly structured cellular materials. Because of their anisotropic nature, spherical indentation deformation leads to a 3-fold symmetric residual indent according to AFM as well as a modulus-relative density scaling exponent of 1.26, less sensitive than conventional foams that tend to be bending dominated. Moreover, the modulus of nanoframes does not vary monotonically with their $\rho_R$, instead the modulus exhibits a transition point near $\rho_R$ = 0.65, and the energy dissipation is also seen to transition at this same $\rho_R$. The energy dissipation characteristics during indentation are studied with numerical simulations. All nanoframes exhibit quite large values of energy dissipation on the order of MJ/m$^3$. Moreover, reducing $\rho_R$ to as low as 0.50 allows the nanoframe to dissipate 25% more energy per unit volume than for a $\rho_R$ of 0.75. In this situation, "less (material) is more (energy absorption)". The estimated energy absorption per volume in the present nanoframes is already comparable to the highest values achieved in conventional polymer foams but at a far smaller strain. We utilize simulation of representative volume elements of the nanoframe microstructures to identify the deformation mechanisms underlying the transition in modulus and dissipation with $\rho_R$ as well as underlying the remarkable energy dissipation per unit volume achieved in these structures. These simulations find a transition from shear-compression combined deformation to shear-dominant one as $\rho_R$ is decreased below 0.65; these same deformation modes provide the enhanced energy dissipation. These mechanisms are in contrast to the typical bending and buckling modes observed in more conventional cellular structures and suggest alternative microstructural designs for achieving and optimizing energy dissipation. Although we have demonstrated the enhancement of mechanical properties of nanoporous materials using a single interference litho-

graphic configuration, the results suggest that future structural materials may be further optimized for specific conditions.

**Supporting Information Available.** Fabrication of samples and determination of relative density of nanoframes. This material is available free of charge via the Internet at http://pubs.acs.org.

## REFERENCES AND NOTES

(1) Ishizaki, K.; Komarneni, S.; Nanko, M. *Porous Materials: Process technology and applications*; Kluwer Academic Publishers: Dordrecht, 1998.

(2) Ashby, M. F.; Evans, A. G.; Fleck, N. A.; Gibson, L. J.; Hutchinson, J. W.; Wadley, H. N. G. *Metal Foams: A Design Guide*; Butterworth-Heinemann: Boston, 2000.

(3) Gibson, L. J.; Ashby, M. F. *Cellular solids*, 2nd ed.; Cambridge University Press: Cambridge, 1997.

(4) Fan, H.; Hartshorn, C.; Buchheit, T.; Tallant, D.; Assink, R.; Simpson, R.; Kissel, D. J.; Lacks, D. J.; Torquato, S.; Brinker, C. J. *Nat. Mater.* **2007**, *6*, 418–423.

(5) Biener, J.; Hodge, A. M.; Hayes, J. R.; Volkert, C. A.; Zepeda-Ruiz, L. A.; Hamza, A. V.; Abraham, F. F. *Nano Lett.* **2006**, *6*, 2379–2382.

(6) Zhu, J.; Peng, H. L.; Marshall, A. F.; Barnett, D. M.; Nix, W. D.; Cui, Y. *Nat. Nanotechnol.* **2008**, *3*, 477–481.

(7) Weissmuller, J.; Viswanath, R. N.; Kramer, D.; Zimmer, P.; Wurschum, R.; Gleiter, H. *Science* **2003**, *300*, 312–315.

(8) Joannopoulos, J. D.; Meade, R. D.; Winn, J. N. *Photonic crystals*: Princeton University Press: Princeton, 1995.

(9) Campbell, M.; Sharp, D. N.; Harrison, M. T.; Denning, R. G.; Turberfield, A. J. *Nature* **2000**, *404*, 53–56.

(10) Lee, J. H.; Kim, Y. S.; Constant, K.; Ho, K. M. *Adv. Mater.* **2007**, *19*, 791–794.

(11) Garin, M.; Trifonov, T.; Rodriguez, A.; Alcubilla, R. *Appl. Phys. Lett.* **2007**, *91*, 181901.

(12) Yang, S. X.; Page, J. H.; Liu, Z. Y.; Cowan, M. L.; Chan, C. T.; Sheng, P. *Phys. Rev. Lett.* **2004**, *93*, 024301.

(13) Jang, J. H.; Ullal, C. K.; Gorishnyy, T.; Tsukruk, V. V.; Thomas, E. L. *Nano Lett.* **2006**, *6*, 740–743.

(14) Moon, J. H.; Yang, S. *Chem. Rev.* **2010**, *110*, 547–574.

(15) Ryoo, R.; Joo, S. H.; Kruk, M.; Jaroniec, M. *Adv. Mater.* **2001**, *13*, 677–681.

(16) Miklyaev, Y. V.; Meisel, D. C.; Blanco, A.; Freymann, G. v.; Busch, K.; Koch, W.; Enrich, C.; Deubel, M.; Wegener, M. *Appl. Phys. Lett.* **2003**, *82*, 1284–1286.

(17) Jeon, S.; Park, J.-U.; Cirelli, R.; Yang, S.; Heitzman, C. E.; Braun, P. V.; Kenis, P. J. A.; Rogers, J. A.; Murray, C. A. *Proc. Nat. Acad. Sci. U.S.A.* **2004**, *101*, 12428–12433.

(18) Hogg, P. J. *Science* **2006**, *314*, 1100–1101.

(19) Jang, J.-H.; Ullal, C. K.; Choi, T.; Lemieux, M. C.; Tsukruk, V. V.; Thomas, E. L. *Adv. Mater.* **2006**, *18*, 2123–2127.

(20) Choi, T.; Jang, J.-H.; Ullal, C. K.; LeMieux, M. C.; Tsukruk, V. V.; Thomas, E. L. *Adv. Funct. Mater.* **2006**, *16*, 1324–1330.

(21) Wang, L.; Boyce, M. C.; Wen, C.-Y.; Thomas, E. L. *Adv. Funct. Mater.* **2009**, *19*, 1343–1350.

(22) Wang, Z.; Li, F.; Ergang, N. S.; Stein, A. *Chem. Mater.* **2006**, *18*, 5543–5553.

(23) Juodkazis, S.; Mizeikis, V.; Seet, K. K.; Misawa, H.; Wegst, U. G. K. *Appl. Phys. Lett.* **2007**, *91*, 241904.

(24) Maldovan, M.; Ullal, C. K.; Jang, J. H.; Thomas, E. L. *Adv. Mater.* **2007**, *19*, 3809–3813.

(25) Lorenz, H.; Despont, M.; Fahrni, N.; Brugger, J.; Vettiger, P.; Renaud, P. *Sens. Actuators, A* **1998**, *64*, 33–39.

(26) Schwartz, M. M. *Composite materials handbook*; McGraw-Hill: New York, 1992.

(27) Meisel, D. C.; Diem, M.; Deubel, M.; Perez-Willard, F.; Linden, S.; Gerthsen, D.; Busch, K.; Wegener, M. *Adv. Mater.* **2006**, *18*, 2964–2968.

(28) Zhu, X. L.; Xu, Y. G.; Yang, S. *Opt. Express* **2007**, *15*, 16546–16560.

(29) Ho, P. K. H.; Thomas, D. S.; Friend, R. H.; Tessler, N. *Science* **1999**, *285*, 233–236.

(30) Oliver, W. C.; Pharr, G. M. *J. Mater. Res.* **1992**, *7*, 1564–1583.

(31) Fisher-Cripps, A. C. *Nanoindentation*, 2nd ed.; Springer: New York, 2004.

(32) Ashby, M. F. *Philos. Trans. R. Soc. London, Ser. A* **2006**, *364*, 15–30.

(33) Woignier, T.; Phalippou, J.; Vacher, R. *J. Mater. Res.* **1989**, *4*, 688–692.

(34) Gibson, L. J.; Easterling, K. E.; Ashby, M. F. *Proc. R. Soc. London, Ser. A* **1981**, *377*, 99–117.

(35) Gurson, A. L. *J. Eng. Mater.* **1977**, *99*, 2–15.

(36) Garboczi, E. J.; Day, A. R. *J. Mech. Phys. Solids* **1995**, *43*, 1349–1362.